OPTICA

Hardware-algorithm collaborative computing with photonic spiking neuron chip based on an integrated Fabry–Perot laser with a saturable absorber

Shuiying Xiang,[1,*,†] Yuechun Shi,[2,3,7,†] Xingxing Guo,[1] Yahui Zhang,[1] Hongji Wang,[3] Dianzhuang Zheng,[1] Ziwei Song,[1] Yanan Han,[1] Shuang Gao,[1] Shihao Zhao,[1] Biling Gu,[1] Hailing Wang,[4] Xiaojun Zhu,[5] Lianping Hou,[6] Xiangfei Chen,[3] Wanhua Zheng,[4] Xiaohua Ma,[1] and Yue Hao[1]

[1]State Key Laboratory of Integrated Service Networks, State Key Discipline Laboratory of Wide Bandgap Semiconductor Technology, Xidian University, Xi'an 710071, China
[2]Yongjiang Laboratory, No. 1792 Cihai South Road Ningbo, Ningbo 315202, China
[3]Key Laboratory of Intelligent Optical Sensing and Manipulation, Ministry of Education, the National Laboratory of Solid State Microstructures, the College of Engineering and Applied Sciences, Institute of Optical Communication Engineering, Nanjing University, Nanjing 210023, China
[4]Laboratory of Solid-State Optoelectronics Information Technology, Institute of Semiconductors, Chinese Academy of Sciences, Beijing 100083, China
[5]School of Information Science and Technology, Nantong University, Nantong, Jiangsu 226019, China
[6]James Watt School of Engineering, University of Glasgow, Glasgow, G12 8QQ, UK
[7]e-mail: yuechun-shi@ylab.ac.cn
*Corresponding author: syxiang@xidian.edu.cn

Received 21 June 2022; revised 4 December 2022; accepted 11 December 2022; published 24 January 2023

Photonic neuromorphic computing has emerged as a promising approach to building a low-latency and energy-efficient non-von Neuman computing system. A photonic spiking neural network (PSNN) exploits brain-like spatiotemporal processing to realize high-performance neuromorphic computing. However, the nonlinear computation of a PSNN remains a significant challenge. Here, we propose and fabricate a photonic spiking neuron chip based on an integrated Fabry–Perot laser with a saturable absorber (FP-SA). The nonlinear neuron-like dynamics including temporal integration, threshold and spike generation, a refractory period, inhibitory behavior and cascadability are experimentally demonstrated, which offers an indispensable fundamental building block to construct the PSNN hardware. Furthermore, we propose time-multiplexed temporal spike encoding to realize a functional PSNN far beyond the hardware integration scale limit. PSNNs with single/cascaded photonic spiking neurons are experimentally demonstrated to realize hardware-algorithm collaborative computing, showing the capability to perform classification tasks with a supervised learning algorithm, which paves the way for a multilayer PSNN that can handle complex tasks.

https://doi.org/10.1364/OPTICA.468347

1. INTRODUCTION

Current conventional electronic processors based on von Neumann's architecture have more and more difficulty maintaining Moore's law. Inspired by the network architecture and principles of the human brain, neuromorphic computing has become one of the promising candidates to overcome the von-Neumann bottleneck to handle certain tasks such as pattern recognition, nonlinear optimization and learning, big data analysis, and decision-making [1]. Compared to the conventional continuous-value-based artificial neural network (ANN) and the convolutional neural network (CNN), the brain-inspired spiking neural network (SNN) provides a more biologically plausible way to implement neuromorphic computing and is believed to be much more powerful and have lower power consumption due to its rich temporal information and event-driven manner [2]. In recent years, significant progress has been achieved in electronic neuromorphic computing processors [3–5], such as SpiNNaker [6], Neurogrid [7], TrueNorth [8], Darwin [9], Loihi [10], and Tianjic [11], but they suffer from the limitations of computational speed and power consumption.

As an alternative, photonic technology offers much promise for next-generation neuromorphic processers, due to fascinating advantages such as high speed, wide bandwidth, massive parallelism, and low power consumption [12–18]. Free-space [19,20] and the integrated photonics architectures [15,16] are two mainstream approaches for the photonic implementation of

neural networks. Due to the potential of a compact size and high reliability, an integrated photonics architecture is a promising approach and significant advancements have been achieved in recent years [21–29]. To use integrated photonics for neuromorphic computing, linear and nonlinear computation elements are indispensable fundamental building blocks of equal importance. The linear computation was successfully realized optically by a Mach–Zehnder interferometer (MZI) [21,30,31], microring resonator (MRR) weight bank [22], phase-change material (PCM) integrated on a waveguide [23,24], and a semiconductor optical amplifier (SOA) [27]. However, among the majority of the existing photonic neural network chips, the nonlinear computation was implemented electronically rather than optically [21,24,27–31]. Thus, the optical implementation of nonlinearity remains one of the most challenging for optical neural networks.

A photonic spiking neural network (PSNN) has been demonstrated that can solve pattern recognition tasks, sound detection, and recognition of handwritten digits from the Modified National Institute of Standards and Technology (MNIST) database [25,26,32–34]. In a PSNN, the nonlinear computation is accomplished by the photonic spiking neuron. The spiking neuron is much more powerful than the continuous-value nonlinear activation due to the rich information represented with spikes based on the spatiotemporal processing mechanism. So far, the optical spiking neurons have been predicted numerically or demonstrated experimentally based on discrete devices [35–39] and integrated schemes [40–46]. In addition, inspired by the Izhikevich model, event-driven optoelectronic laser spiking neurons without a requirement for a continuous laser pump have been recently proposed, which offers exceptionally high energy efficiency [33]. These approaches, however, also face some limitations. For instance, the PCM-based spiking neuron lacks a temporal integration function, which is crucial to spike processing [23,42]. The output power of a micropillar laser neuron is relatively low, which may require additional amplification to compensate for the loss when applied to a multilayer or deep PSNN [43,44]. The integrated distributed feedback laser neuron requires optic-electronic conversion, which may cause increased system complexity and power consumption [45]. To pave the way for the practical application of PSNNs, it is still highly desirable to explore a novel photonic spiking neuron chip that can take full advantage of the temporal encoding feature and can be easily applied to multilayer or deep PSNNs to handle complex tasks.

Here, for what we believe, to the best of our knowledge is the first time, we have proposed and fabricated a photonic spiking neuron chip based on an integrated Fabry–Perot laser with an intracavity saturable absorber (FP-SA) that could form an integral part of the PSNN hardware. Besides, to avoid the currently available photonics integration scale limit, we proposed time-multiplexed temporal spike encoding in different time windows by using a single photonic spiking neuron, which enabled the implementation of a large-scale PSNN far beyond the hardware integration scale limit. Furthermore, hardware-algorithm collaborative computing based on a PSNN consisting of a single and two cascaded photonic spiking neurons were experimentally demonstrated to perform a pattern classification task with a modified supervised learning algorithm. We believed this represents a major step forward toward the practical application of PSNNs. Our experimental demonstrations present a promising avenue toward hardware–software co-design and optimization of large-scale multilayer PSNNs to solve complex tasks, and could be promising for wide applications such as in machine learning, artificial intelligence, data centers, edge computation, and autonomous driving.

2. EXPERIMENTAL SETUP AND METHOD

A. Design and Fabrication of Integrated FP-SA Laser Chip

The nonlinear computation functions are accomplished by the proposed photonic spiking neuron, which mainly include temporal integration, threshold, spike generation, and a refractory period, as presented in Fig. 1(a). In our work, the photonic spiking neuron chip based on the integrated FP-SA was designed, optimized, and fabricated. The integrated FP-SA laser chip includes two electrical isolation sections; i.e., a gain region and a saturable absorber (SA) region. Figure 1(b) shows the microscopic image of the fabricated laser. The total length of the chip is $L_{\text{cavity}} = 1500\ \mu\text{m}$, the width of the laser chip is 300 μm, and the ridge waveguide width is 2.5 μm. After optimization, we designed and fabricated the devices with four different SA lengths: $L_{\text{SA}} = 25\ \mu\text{m}$, 30 μm, 75 μm, and 90 μm. The SA section side facet and gain section side facet are coated with reflections of 95% and 30%, respectively. For the FP-SA with different SA lengths, we packaged several devices to demonstrate uniformity. The material used in this work is a p-i-n diode structure grown based on the AlGaInAs/InP material system with an epitaxial layer structure similar to that described in [47].

B. Time-Multiplexed Spatiotemporal Spike Encoding Mechanism

To take advantage of the temporal information of SNN, we proposed time-multiplexed temporal spike encoding with a single photonic spiking neuron. Note that, different from the time-multiplexing concept that reuses the photonic neural chip many times [28,29], a time-multiplexed spike is realized by temporal encoding in different time windows by using the photonic spiking neuron chip only one time. The classification task is to distinguish four simple number patterns (i.e., 1, 2, 3, and 4), with a 5×4 pixel matrix, as presented in Fig. 1(c). As shown in Fig. 1(d), we consider a small PSNN with four presynaptic (PRE) neurons and four postsynaptic (POST) neurons. Each column in the matrix of five pixels is encoded with a PRE neuron (see Supplement 1, Note 1, for more detail). All the PRE spikes are weighted and then propagated to four POSTs. The weight matrix consists of ω_{ij}, which represents the synaptic weight between the j-th PRE and the i-th POST. Note that the weights are trained with a supervised algorithm in a computer, and only the inference process is accomplished in the hardware in the present work.

The spatiotemporal pattern of the target response is shown in Fig. 1(e), and is defined as target = [1, 0, 0, 0; 0, 1, 0, 0; 0, 0, 1, 0; 0, 0, 0, 1]. Here, one row represents one POST, and one column denotes the target response of four POSTs corresponding to a specific input pattern. For simplicity, we use 1 and 0 to indicate that the POST fires and doesn't fire a spike, respectively. For instance, for pattern "1", the target is that POST1 fires a spike, and the rest three POSTs do not fire a spike. Thus, the first column [1, 0, 0, 0] represents the target response of pattern "1". For pattern "2", the target is that only POST2 fires a spike, and the target response corresponds to the second column [0, 1, 0, 0]. Similarly, the target

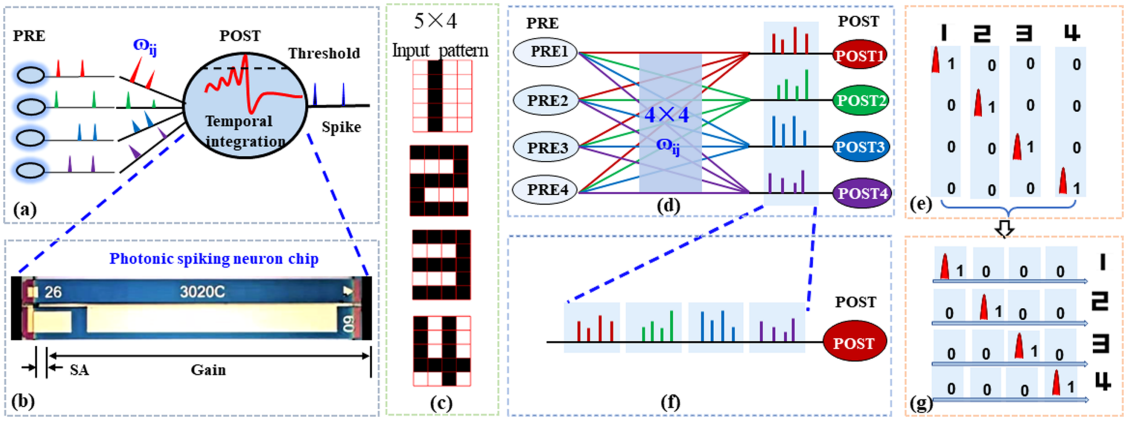

Fig. 1. Operational principle of PSNN for pattern recognition. (a) Nonlinear computation mechanism of a photonic spiking neuron chip and (b) chip layout of the integrated FP-SA chip. (c) Input patterns with 5 × 4 pixel matrix. (d) PSNN with four input nodes and four output nodes and (f) proposed time-multiplexed spike encoding to realize the spatiotemporal spike encoding with a single FP-SA neuron. (e) Spatiotemporal target output response for recognition of different input patterns and (g) target output response for different input patterns. PRE, pre-synaptic spiking neuron; POST, post-synaptic spiking neuron. ω_{ij} is the synaptic weight between the j-th PRE and the i-th POST, which is trained with a supervised learning algorithm.

responses of patterns "3" and "4" correspond, respectively, to the third column [0, 0, 1, 0] and the fourth column [0, 0, 0, 1].

In our proposed scheme, we used only one POST neuron to achieve the same functions of four POSTs of the entire layer of the PSNN by the time-multiplexed temporal spike encoding mechanism. Note that each hardware connection represents four different weights; namely, the synaptic weights must be dynamically updated in different time windows. As presented in Fig. 1(f), one POST neuron has four response time windows corresponding to four virtual POSTs to respond to a specific input pattern. For example, as shown in Fig. 1(g), for pattern "1", the POST only fires a spike in the first time window and does not fire in the rest of the three time windows. Thus, the response of the POST can be represented as [1, 0, 0, 0]. For pattern "2", "3", and "4", the POST only fires a spike in the second, third, and fourth time windows, and the response of the POST can be denoted, respectively, as [0, 1, 0, 0], [0, 0, 1, 0], and [0, 0, 0, 1].

C. Experimental Setup for Photonic Spiking Neuron

The experimental setup of an FP-SA neuron to emulate the neuron-like dynamics is presented in Fig. 2(a). An arbitrary waveform generator (AWG; AWG70001A, Tektronix) produced the electronic stimulus. A tunable laser (TL; AQ2200-136 TLS module, Yokogawa) provided the optical carrier. The electro-optical conversion was realized with an Mach–Zehnder modulator (MZM). Here, the half-wave voltage of the MZM was 1.9 V. The modulated optical stimulus was then injected into the facet of the gain section of the FP-SA via an optical circulator. The gain region was forward biased with a laser diode controller (LDC; LDC3724B, ILX Lightwave) that provided low-noise bias current and precise temperature control. The SA was reverse biased with the voltage source (VS). A variable optical attenuator (VOA) was used to adjust the power of the injected signal from the MZM and erbium-doped fiber amplifier (EDFA). Here, the EDFA is used to compensate for the relatively high insertion loss (8.3 dB) of the available MZM in our experiment. The polarization controllers (PC1 and PC2) were employed to match the polarization state. The output of the FP-SA neuron was analyzed by an optical spectrum analyzer (OSA; Q8384, Advantest), was detected by a photodetector (PD; 11982A, Agilent/HP) and then recorded by an oscilloscope (OSC; DSOV334A, Keysight) and an RF spectrum analyzer (FSW85, Rohde & Schwarz).

In the experiment, when the temperature was fixed at 25°C, the power current (PI) curves for free-running FP-SA lasers are presented in Figs. 2(b1) and 2(b2) under different cases of reverse bias of the SA region. The PI curves for four FP-SA lasers with different L_{SA} are similar. Here, only the PI curves for FP-SA with $L_{SA} = 25$ μm and $L_{SA} = 30$ μm are presented. For both devices, it can be seen that the threshold of the gain current is $I_G = 30$ mA for a reverse voltage $V_{SA} = 0$ V. An increase in the SA reverse voltage raises the threshold current and reduces the slope efficiency as a result of an increase in the interband and exciton absorption.

D. Model and Algorithm

To design the supervised learning algorithm and realize the hardware-algorithm co-design, we use rate equations based on the Yamada model [25,26]:

$$\frac{dS_{i,o}}{dt} = \Gamma_a g_a (n_a - n_{0a}) S_{i,o} + \Gamma_s g_s (n_s - n_{0s}) S_{i,o} - \frac{S_{i,o}}{\tau_{\text{ph}}} + \beta B_r n_a^2, \tag{1}$$

$$\frac{dn_a}{dt} = -\Gamma_a g_a (n_a - n_{0a})(S - \Phi_{\text{pre},i} - \Phi_{\text{post},o}) - \frac{n_a}{\tau_a} + \frac{I_a}{e V_a}, \tag{2}$$

$$\frac{dn_s}{dt} = -\Gamma_s g_s (n_s - n_{0s}) S_{i,o} - \frac{n_s}{\tau_s} + \frac{I_s}{e V_s}, \tag{3}$$

where $S_{i,o}$ represents the photon density in the cavity. The subscripts i and o represent the PRE and POST neuron, respectively. n_a (n_s) is the carrier density in the gain (absorber) region. $\Phi_{\text{pre},i}$ represents the external stimulus signal received by a PRE neuron. $\Phi_{\text{post},o}$ denotes the stimulus signal received by a POST neuron, which is the weighted sum of the output spikes from the neurons in the previous layer. The parameters used in simulations are the same as those in [26] (see Supplement 1, Note 2, for more detail). Note that, according to our experimental measurements for different pattern recognition tasks, we find that even with these simple single-mode rate equations, the trained weight can be accurately

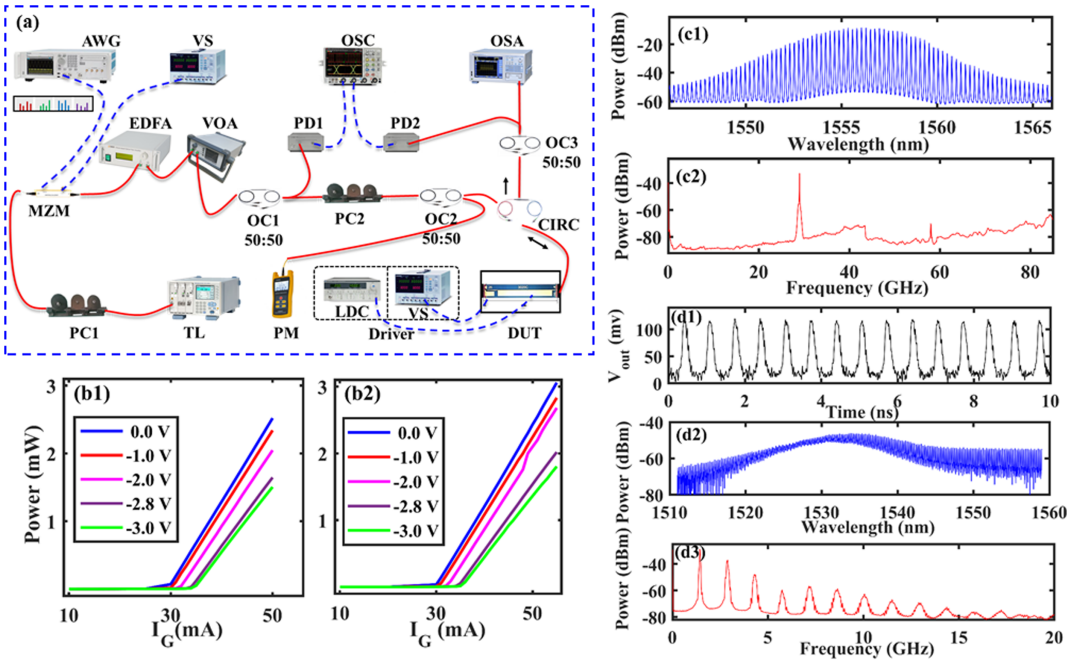

Fig. 2. Experimental setup, PI curves, and the self-pulsation output characteristics of the FP-SA neuron. (a) Experimental setup to test the FP-SA neuron. AWG, arbitrary waveform generator; VS, voltage source; TL, tunable laser; OI, optical isolator; VOA, variable optical attenuator, PC1 and PC2, polarization controllers; MZM, Mach–Zehnder modulator; OC1 and OC2, optical couplers; CIRC, circulator; PD1 and PD2, photodetectors; PM, power meter; OSC, oscilloscope; OSA, optical spectrum analyzer; LDC, laser diode controller; and DUT, device under test. PI curve of FP-SA with (b1) $L_{SA} = 25$ μm and (b2) with $L_{SA} = 30$ μm. (c1) Optical spectra and (c2) RF spectrum of free-running FP-SA with $L_{SA} = 75$ μm, $I_G = 95$ mA, $V_{SA} = -3.05$ V. The output power is 5.6 mW for the mode-locked regime. (d1) Time series, (d2) optical spectra, and (d3) RF spectrum of free-running FP-SA with $I_G = 100$ mA, $V_{SA} = -4.49$ V. The output power is 2.6 mW for the Q-switching regime (see Visualization 1 and Visualization 2).

mapped to the multimode FP-SA hardware to obtain successful pattern recognition, which is helpful to reduce the training time.

During the PSNN training process, a modified tempotron-like ReSuMe supervised learning algorithm is used [48,49], and can be described as

$$\Delta\omega_{ij} = \begin{cases} \sum_{t_i \le t_{\max}} K(t_{\max} - t_i), & \text{if } n^d = 1,\ n^o = 0 \\ -\sum_{t_i \le t_{\text{out}}} K(t_{\text{out}} - t_i), & \text{if } n^d = 0,\ n^o = 1 \\ 0, & \text{if } n^d = n^o \end{cases}, \tag{4}$$

$$\omega_{ij}(x+1) = \omega_{ij}(x) + \omega_f \times \Delta\omega_{ij}. \tag{5}$$

The K function can be expressed as

$$K(t) = V_0 \cdot \left(\exp\left(\frac{-t}{\tau_m}\right) - \exp\left(\frac{-t}{\tau_s}\right) \right), \tag{6}$$

in which $V_0 = 2.1165$, $\tau_m = 1$ ns, and $\tau_s = \tau_m/4$. The learning window only considers spikes $t_i \le t$. $\omega_{ij}(x)$ and $\omega_{ij}(x+1)$ are the synapse weights at the x-th and $(x+1)$-th learning epochs, respectively. ω_f is the learning rate and is set as 0.4×10^8. It denotes the maximum change in synaptic efficacies. $\Delta\omega_{ij}$ represents the weight update amount. n^d and n^o are the number of spikes, respectively, from the desired and the actual output spike trains. The algorithm updates its weights whenever the neuron fails to respond as the same desired state as the teacher. When $n^d = 1$ is presented to the POST, it should fire a spike. However, once the actual response of POST is no spike ($n^o = 0$), the synaptic weight should be strengthened. On the other hand, when $n^d = 0$ is presented to the POST, it should keep silent. If the actual response of POST fires a spike ($n^o = 1$), the synaptic weight should be depressed. Here, the shape of the learning window follows kernel K and the changing amount of the weight depends on the time difference between t_i, t_{out} and $t_{\max}$, in which t_i is the pre-synaptic spike time, t_{out} is the actual output spike time, and $t_{\max}$ denotes the time at which the neuron reaches its maximum output power value in the time domain.

3. RESULTS

A. Self-Pulsation Regimes of FP-SA

Note, for the free-running FP-SA, when the gain current I_G and reverse voltage V_{SA} are sufficiently large, two different stable pulse operation regimes can be observed; i.e., pure mode-locking and self-pulsation regions. For example, for the FP-SA with $L_{SA} = 75$ μm, when $I_G = 95$ mA and $V_{SA} = -3.05$ V, the optical spectrum and RF spectrum are shown in Figs. 2(c1) and 2(c2). Multiple longitudinal modes with clear and deep modulation (maximum modulation >45 dB) can be seen, and the mode spacing is about 0.24 nm. This corresponds to a frequency spacing of 28.9 GHz, which is equal to $c/(2n_g\, L_{\text{cavity}})$. Here, $n_g = 3.46$ is the group refractive index of the ridge waveguide of the FP-SA chip, and c is the speed of light in a vacuum. The RF spectrum shows that the FP-SA emits pulses with a fundamental frequency of 28.9 GHz and their high-order harmonic components. When the reverse voltage is fixed at $V_{SA} = -3.05$ V, the FP-SA emits around 28.9 GHz pulse trains for the gain current range from 89.2 to 98 mA. These spectra properties indicate that the FP-SA operates at the pure mode-locking regime with 100% modulation. In addition, when we further increase the I_G and V_{SA}, the FP-SA enters the self-pulsation regime. For $V_{SA} = -4.49$ V, the frequency varies from 1.49 to 1.95 GHz when I_G is increased from 100 to 120 mA,

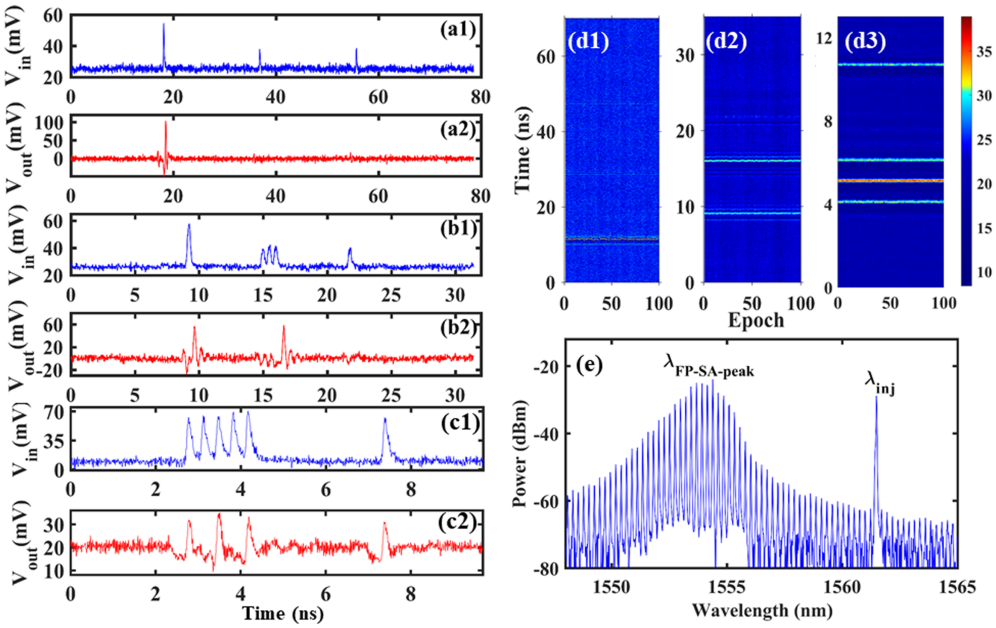

Fig. 3. Experimental demonstration of neuron-like dynamics and the corresponding optical spectrum: (a) threshold, (b) temporal integration, and (c) refractory period. (a1)–(c1) represent the stimulus signal of the laser neuron, (a2)–(c2) denote the response of the FP-SA neuron. Temporal maps plotting the response of laser neuron to the arrival of 100 consecutive external stimuli, (d1) corresponds to stimulus in (a1), (d2) corresponds to stimulus in (b1), and (d3) corresponds to stimulus in (c1). (e) The optical spectra for the FP-SA operate as a photonic spiking neuron. $I_G = 56.2$ mA, $V_{SA} = -3$ V, $\lambda_{inj} = 1561.48$ nm, and $P_{inj} = 75.15$ μW for testing the threshold and temporal integration, and $P_{inj} = 117$ μW for testing the refractory period (see Visualization 3 and Visualization 4).

which is due to the Q-switching mechanism. The time series, optical spectrum, and RF spectrum are presented in Figs. 2(d1)–2(d3) for $I_G = 100$ mA. Compared to the pure mode-locking, the optical spectrum widens while its modulation depth decreases. In our experiments, we find that the two different pulse regimes are more critical to the V_{SA}, but can be maintained for a relatively wide range of I_G that is greater than the pulse threshold.

For all the considered FP-SA lasers, two pulse regimes can be observed, but with slightly different I_G and V_{SA} ranges. Note that, to emulate the neuron-like dynamics with the FP-SA, the bias current and reverse voltage should be set below the Q-switching pulse threshold. In such a case, a small external input light perturbations can trigger the FP-SA to produce a single pulse [50].

B. Nonlinear Neuron-Like Dynamics of Photonic Spiking Neuron Based on the FP-SA

We designed the perturbation signal generated by the AWG to demonstrate the complex nonlinear neuron-like dynamics of the photonic spiking neuron. Here, we only present the results for the FP-SA with $L_{SA} = 30$ μm. Note that we found that the results for other FP-SAs with different SA lengths are similar through extensive experimental measurements. Nonetheless, a FP-SA with larger SA length usually requires higher I_G due to stronger absorption. As shown in Figs. 3(a1) and 3(a2), the perturbation signal includes three pulses with different power. Only the first injected pulse triggers the FP-SA neuron to generate a neuron-like spike. The responses of the FP-SA neuron to the second and the third perturbation pulses are negligible, which indicates the excitability threshold. We also designed three types of pulse stimuli to demonstrate the temporal integration effect, as shown in Figs. 3(b1) and 3(b2). The first pulse with a high input power elicits a spike generation of the FP-SA neuron, the second pulse burst with three closely spaced weak pulses with an interspike interval (ISI) of 0.5 ns, also triggers a spike generation, while the third single sub-threshold perturbation pulse does not elicit the response spike. In other words, even a single sub-threshold pulse cannot reach the spike threshold, the three closely spaced sub-threshold pulses are temporally integrated and thus exceed the threshold, which demonstrates the temporal integration function of the FP-SA neuron. As presented in Figs. 3(c1) and 3(c2), we designed and generated a burst of pulse (ISI is 0.4 ns) with a relatively high intensity and a separate single reference pulse. We found that the first perturbation pulse can elicit a response spike, indicating that the single perturbation pulse power exceeds the threshold. However, the second perturbation pulse cannot trigger another response spike because the gain is not fully recovered in the gain section [51]. The bursts of five pulses only trigger three response spikes, which indicates that the refractory period is between 0.4 and 0.8 ns [43]. The refractory period means that the spiking neuron cannot produce another response spike to the stimulus in a short time due to the carrier recovery process, if it just responded with a spike to the preceding stimulus. The refractory period is associated with the carrier recovery process, and the values we observed also included 0.3, 0.4, and 0.5 ns under different conditions in our experiments (see details in Supplement 1, Note 3). Note that the maximum spiking response rate (~3.3 GHz) is limited by the inverse of the refractory period. Obviously, the response speed is much faster than the biological counterpart. In Figs. 3(d1)–3(d3), we further present the experimental color-coded temporal maps plotting superimposed time series of the responses corresponding to 100 consecutive arriving stimuli events. For the three cases, the same spiking response is obtained for every single one of the 100 incoming stimuli. Hence, reproducible spiking responses can be

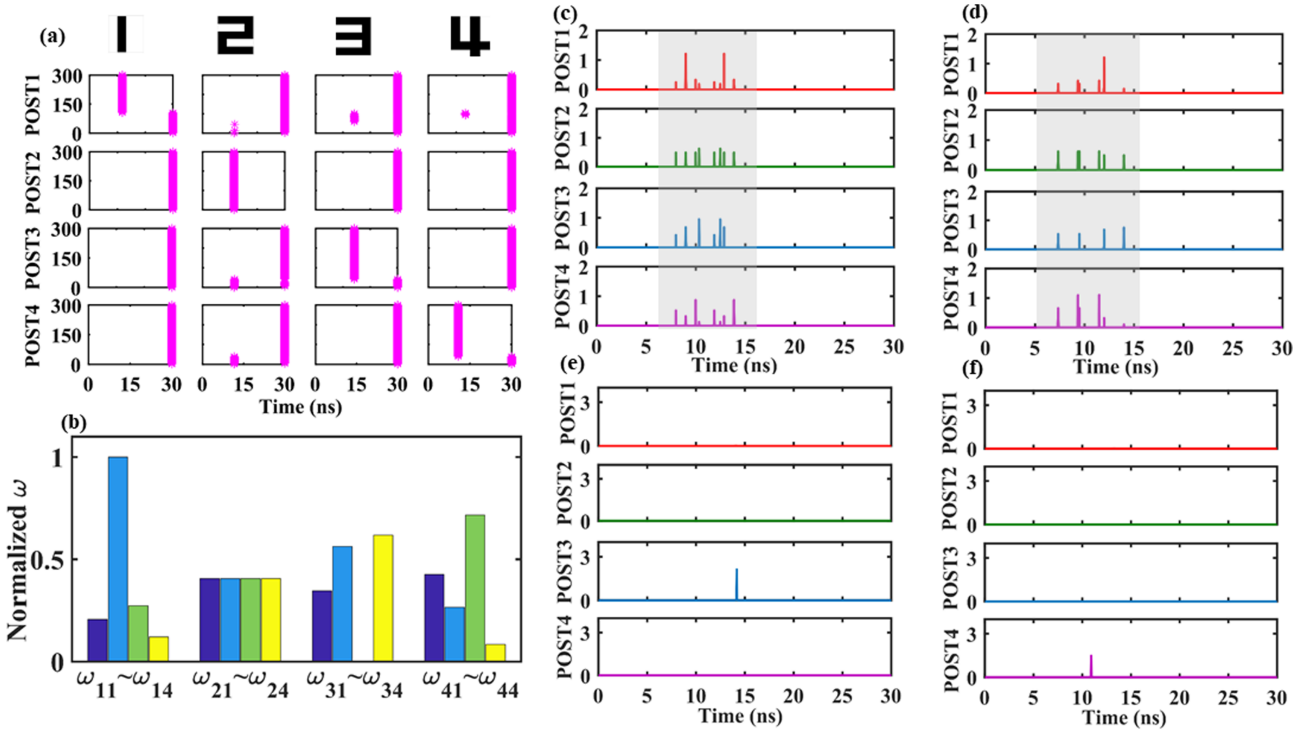

Fig. 4. Training process and simulation results based on the PSNN. (a) Training process for each pattern, (b) Weight after training convergence, (c) and (d) Inputs of each POST for the pattern "3" and "4", respectively, and (e) and (f) Response of each POST corresponding to (c) and (d). ω_{ij} denotes the synaptic connection weight between j-th PRE and i-th POST.

obtained in our fabricated FP-SA neuron. In addition, the inhibitory dynamics is also demonstrated, as detailed in Supplement 1, Note 4. The optical spectrum for the optically injected FP-SA that operates as a photonic spiking neuron is further presented in Fig. 3(e). Here, the injection wavelength is away from the peak wavelength. Note that the neuron-like dynamics can be observed when the injection wavelength λ_{inj} matches or is slightly longer than one of longitudinal mode wavelengths of the FP-SA that is away from the peak region. Provided that the injected wavelength satisfies the above-mentioned condition, the minimum injected power required to realize the neuron-like dynamics is relatively high for a larger separation between the injection wavelength and the peak wavelength. An additional discussion can be found in Supplement 1, Note 5. Note that, external optical injection could also lead to excitability based on homoclinic bifurcation in the injection locking range [52], which also motivates further investigation on the neuron-like dynamics of FP-SA based on the homoclinic bifurcation mechanism.

C. Training Process Based on Modified Supervised Learning Algorithm

The training process and simulation results are shown in Fig. 4 (see details in Supplement 1, Note 6). For this task, the training convergence is achieved at the 106th epochs. Here, the accuracy reached 100% during the training process. For pattern "1" only POST 1 emits a spike, while the rest of the three POSTS emit no spike, and the timing is the maximum of the training window. Similarly, for patterns "2", "3", and "4", the training convergence agrees well with the defined target. The weights after the training convergence are presented in Fig. 4(b). After the training convergence, the spike encoding output of each PRE is multiplied by the trained weight matrix. To intuitively present the insight into the weight process, the weighted signals that are injected into each POST for patterns "3" and "4" are shown in Figs. 4(c) and 4(d). The corresponding responses of each POST for patterns "3" and "4" are shown in Figs. 4(e) and 4(f). Obviously, only POST 3 emits a spike for pattern "3". For pattern "4", only POST 4 generates a spike. Note that, to realize the time-multiplexed temporal spike encoding, as shown in Fig. 1(f), the weighted additions are combined to obtain a single stimulus signal that is imported to the hardware photonic spiking neuron. Because this work focuses on the hardware implementation of a photonic spiking neuron, the combined weighted signal is directly mapped to the output of the AWG.

D. PSNN Hardware Implementation Based on Single FP-SA

After training convergence, the weighted signal for each POST is mapped to a time-multiplexed signal that can be generated by the AWG. The electronic output of the AWG is modulated by the MZM and injected into the fabricated FP-SA to realize a photonic spiking neuron. When the input pattern is "1", the time-multiplexed input for the POST is presented in Fig. 5(a1). As seen in Fig. 5(a2), only one spike appears in the first time window (i.e., "1" state), while the FP-SA laser neuron responds with a low-intensity sub-threshold oscillation during the rest of the time windows (i.e., "0" state), which agrees well with the target output denoted in Fig. 1(e). Because the triggered high-intensity spike in the desired time window can be easily distinguished from the low-intensity response from the of the rest time windows, we regard it as an accurate pattern recognition. A larger power ratio (i.e., $\max.P_1/\max.P_0$) implies a better pattern recognition performance. Hence, pattern "1" is successfully recognized by the

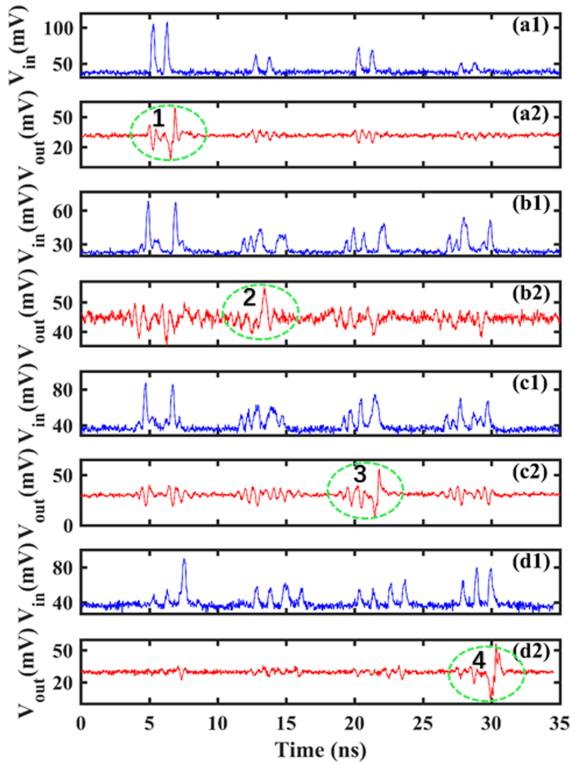

Fig. 5. Response of the fabricated photonic spiking neuron for different input patterns after weight is applied. (a1) Time-multiplexed input of the photonic spiking neuron for pattern "1" and (a2) corresponding response; (b1) and (b2) correspond to pattern "2"; (c1) and (c2) correspond to pattern "3"; and (d1) and (d2) correspond to pattern "4". $I_G = 59.4$ mA and $V_{SA} = -2.503$ V.

spatiotemporal dynamics of the single photonic spiking neuron. When the input pattern is "2", the time-multiplexed weighted addition signal presented in Fig. 5(b1) is quite different from that of pattern "1", and the FP-SA laser neuron responds with a high-intensity spike during the second time window, as shown in Fig. 5(b2). Similarly, as shown in Figs. 5(c1)–5(d2), when the input pattern is "3" or "4", the FP-SA laser neuron responds with a high-intensity spike during the third or fourth time window. Thus, both the temporal integration and threshold properties contribute to the spike generation in a desired time window, and the inference process of the classification task is successfully demonstrated in the hardware. It is worth pointing out here that the hardware-algorithm collaborative computing based on PSNN with time-multiplexed temporal spike encoding is realized for what we believe is the first time, to the best of our knowledge.

Note that the electronic noise is inevitable in the AWG, PD, and OSC, as well as the environment variation and the FP-SA laser neuron's noise, and the same spiking response is obtained for each pattern; thus, the inference process is robust to noise to some degree (see more details in Supplement 1, Note 7).

E. Hardware Implementation of Multilayer PSNN with Two Cascaded Photonic Spiking Neurons

We further cascade two hardware photonic spiking neurons to study the cascadability property and multilayer PSNN. As presented in Fig. 6(a), FP-SA1 represents the first photonic spiking neuron, and FP-SA2 denotes the second photonic spiking neuron. The injection path of the FP-SA1 is simplified, as it has

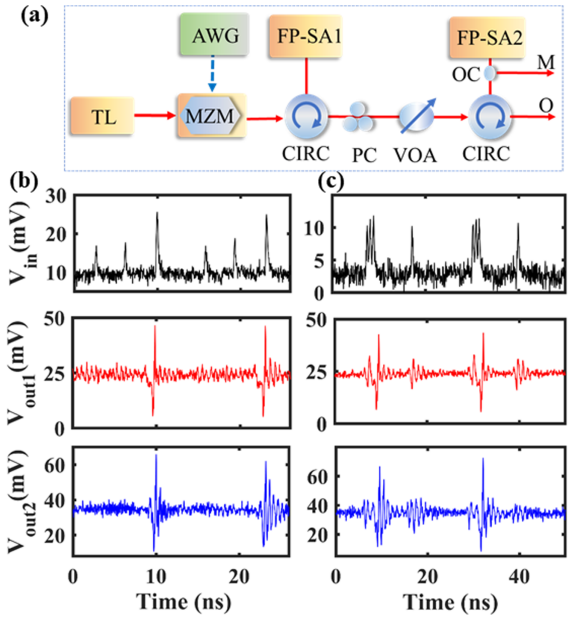

Fig. 6. Cascaded photonic spiking neurons and the cascadability. (a) Schematic diagram of cascaded two hardware photonic spiking neurons. M represents the monitor port of the injected power, O denotes the output port of FP-SA2. The cascadability of (b) the threshold and (c) the temporal integration. V_{in} means the input of FP-SA1, V_{out1} denotes the response of FP-SA1, and V_{out2} represents the response of FP-SA2. For FP-SA1, $I_G = 60.5$ mA and $V_{SA} = -2.34$ V; for FP-SA2, $I_G = 58.4$ mA and $V_{SA} = -2.56$ V.

been described in Fig. 2(a). The output of FP-SA1 is optically injected into FP-SA2, and the injected optical power should be carefully adjusted by a PC and VOA between them to realize the cascadability. A 90:10 optical coupler is further introduced before the FP-SA, and 10% of the injected power is monitored to determine the injected power. Note that two FP-SAs are set to operate in the neuron-like dynamics regime (see Supplement 1, Note 8, for the details of the optical spectra for both FP-SAs). As shown in Figs. 6(b) and 6(c), the neuron-like threshold and temporal integration property can be achieved in both FP-SAs, which demonstrates that the cascadability of a biological neuron is successfully emulated.

With the cascaded configuration, we also consider the pattern recognition tasks. Here, two pattern recognition tasks that include "XDU" and "NJU" images are considered. The input spike encoding and training process are described in detail in Supplement 1, Note 9. The inference performances of "XDU" and "NJU" are presented in Fig. 7. Here, the target responses of POST1, POST2, and POST3 are, respectively, [1, 0, 0], [0, 1, 0], and [0, 0, 1]. After the training convergence, the weight matrix is multiplied by the spike output of PREs, and then the modulated time-multiplexed temporal spike encoding signal is optically injected into the FP-SA1, and the output of FP-SA1 is optically injected into FP-SA2. For both tasks, three input patterns can be successfully recognized by two cascaded photonic spiking neurons based on the FP-SA with a desired spike emission window.

Interestingly, we find that better recognition performance can be achieved by the FP-SA2; that is, the FP-SA2 provides an additional threshold effect, and thus, the spike event in the desired time window (i.e., "1" state) becomes more distinguishable from the rest time windows with subthreshold oscillation or noise level

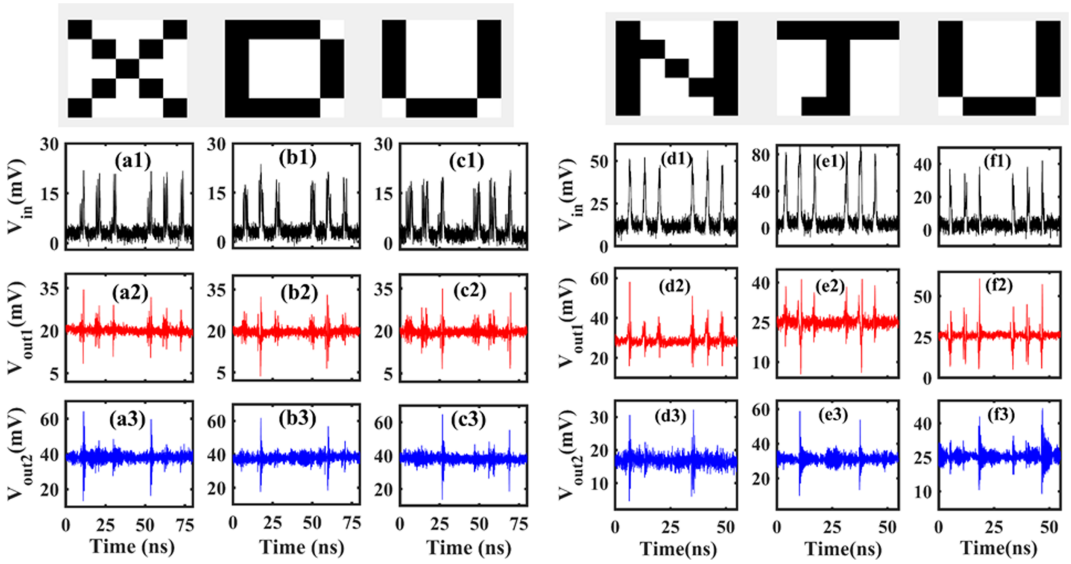

Fig. 7. Pattern recognition of the patterns with cascaded photonic spiking neurons: (a)–(c) "X," "D," and "U," and (d)–(f) "N," "J," and "U." For the XDU task, $I_G = 59$ mA and $V_{SA} = -2.477$ V for FP-SA1, $I_G = 60.7$ mA, and $V_{SA} = -2.409$ V for FP-SA2. For the NJU task, $I_G = 61$ mA and $V_{SA} = -2.434$ V for FP-SA1, $I_G = 62.1$ mA, and $V_{SA} = -2.446$ V for FP-SA2 (see Visualization 5).

fluctuation (i.e., "0" state). On one hand, from the physical perspective, such better neural computation performance may take advantage of the combined saturable absorption effects of two FP-SAs. On the other hand, from the neural network perspective, this may be because the cascaded configuration exhibits a multilayer PSNN because each FP-SA represents an entire layer of spiking neurons with the time-multiplexed temporal spike encoding. Namely, the first FP-SA1 can be regarded as the hidden layer, and FP-SA2 can be regarded as the output layer.

4. DISCUSSION AND CONCLUSION

In summary, we fabricated, what we believe, to the best of our knowledge, is a novel photonic spiking neuron chip based on an integrated FP-SA that has a simple structure and can be easily integrated on large scale with a commercially mature semiconductor process. The controllable and reproducible complex nonlinear neuron-like dynamics such as temporal integration, threshold and spike generation, refractory period, and inhibitory behavior were demonstrated experimentally and are much faster than their biological and electronic counterparts. The proposed approach offers an indispensable fundamental building block to realize the PSNN hardware, and will be a key foundation for large-scale integrated PSNN chips. Furthermore, we proposed time-multiplexed temporal spike encoding to mimic the brain-like spatiotemporal processing, and realized the hardware implementation of the inference process for pattern classification tasks with a single photonic spiking neuron based on a modified supervised learning algorithm. Note that the time-multiplexed temporal spike encoding enabled the implementation of a large-scale functional PSNN far beyond the hardware integration scale limit. A multilayer PSNN with two cascaded photonic spiking neurons was also experimentally realized. Both the cascadability performances and the pattern recognition inference tasks were successfully demonstrated. We believe the first experimental demonstration of hardware-algorithm collaborative computing based on a photonic spiking neuron represents a major step toward the practical application of an integrated PSNN chip, and proves the potential to build a large-scale, multilayer PSNN chip to address complex tasks.

In our experiments, we found that temperature plays a key role in neuro-inspired computing because it determines the frequency detuning between the injected light and the longitudinal mode of the FP-SA laser neuron. Hence, temperature management should be emphasized when considering the large-scale photonic spiking neuron array. To further improve the inference performance, the hardware-software co-design and optimization of the PSNN are highly desirable in a future iteration.

Finally, we also discussed the energy efficiency, spiking processing speed, and potential scalability (see details in Supplement 1, Note 10). The energy efficiency of the FP-SA neuron is estimated at about 7.329 fJ/spike. In electronic approaches, the methods to benchmark based on calculating the conventional multiply-accumulate (MAC) operation show 1300 pJ/MAC in TrueNorth and 226 pJ/MAC in Loihi [33]. In addition, by considering the MZM modulator that accomplishes the weighting function, the calculated energy efficiency is about 5.16 pJ/MAC.

In our experiment, the FP-SA can process an input stimulus pulse with rate of 10 GHz, and its maximum spiking response rate is estimated at about 3.3 GHz, which is the inverse of refractory period. Note that the FP-SA can be easily integrated into a large-scale bar array, which is interesting for real-scale problems. For our fabricated chips, each bar contains about 83 chips; thus, it is promising to realize a large-scale photonic spiking neuron array. The scalability of a photonic spiking neuron array is mainly limited by the available packaging technique. As a further attempt, it is highly desirable to integrate the III-V laser neuron chip with silicon-photonics-based weight devices such as an MRR or an MZI network, or InP-based weight devices such as an SOA. There have been many experimental demonstrations of the vector-matrix multiplication in the past few years [15]. A hybrid III-V/silicon integration may be a promising solution for the implementation of the entire on-chip PSNN [53,54]. In addition, the fast time-varying weight that can be dynamically updated also deserves

further innovation to take full advantage of the time-multiplexed temporal spike encoding mechanism of a photonic spiking neuron.

Funding. National Key Research and Development Program of China (2021YFB2801900, 2021YFB2801902, 2021YFB2801904, 2018YFE0201200); National Natural Science Foundation of China (61974177, 61674119); National Outstanding Youth Science Fund Project of National Natural Science Foundation of China (62022062); Fundamental Research Funds for the Central Universities (JB210114).

Acknowledgment. The authors would like to thank Dr. Jianji Dong, Dr. Qiang Li, and Dr. Cuicui Lu for their helpful discussions.

Disclosures. The authors declare no conflicts of interest.

Data availability. Data underlying the results presented in this paper are not publicly available at this time but may be obtained from the corresponding author upon reasonable request.

Supplemental document. See Supplement 1 for supporting content.

[†]These authors contributed equally to this work.

REFERENCES

1. K. Roy, A. Jaiswal, and P. Panda, "Towards spike-based machine intelligence with neuromorphic computing," Nature **575**, 607–617 (2019).
2. W. Maass, "Networks of spiking neurons: the third generation of neural network models," Neural Netw. **10**, 1659–1671 (1997).
3. R. A. Nawrocki, R. M. Voyles, and S. E. Shaheen, "A mini review of neuromorphic architectures and implementations," IEEE Trans. Electron Dev. **63**, 3819–3829 (2016).
4. C. D. Schuman, T. E. Potok, R. M. Patton, J. D. Birdwell, M. E. Dean, G. S. Rose, and J. S. Plank, "A survey of neuromorphic computing and neural networks in hardware," arXiv arXiv:170506963 (2017).
5. D. Marković, A. Mizrahi, D. Querlioz, and J. Grollier, "Physics for neuromorphic computing," Nat. Rev. Phys. **2**, 499–510 (2020).
6. E. Painkras, L. A. Plana, J. Garside, S. Temple, F. Galluppi, C. Patterson, D. R. Lester, A. D. Brown, and S. B. Furber, "SpiNNaker: A 1-W 18-core system-on-chip for massively-parallel neural network simulation," IEEE J. Solid-State Circ. **48**, 1943–1953 (2013).
7. B. V. Benjamin, P. Gao, E. McQuinn, S. Choudhary, A. R. Chandrasekaran, J. M. Bussat, R. A. Icaza, J. V. Arthur, P. A. Merolla, and K. Boahen, "Neurogrid: A mixed-analog-digital multichip system for large-scale neural simulations," Proc. IEEE **102**, 699–716 (2014).
8. P. A. Merolla, J. V. Arthur, R. Alvarez-Icaza, *et al.*, "A million spiking-neuron integrated circuit with a scalable communication network and interface," Science **345**, 668–673 (2014).
9. J. Shen, D. Ma, Z. Gu, M. Zhang, X. Zhu, X. Xu, Q. Xu, Y. Shen, and G. Pan, "Darwin: a neuromorphic hardware co-processor based on spiking neural networks," Sci. China Inf. Sci. **59**, 1–5 (2016).
10. M. Davies, N. Srinivasa, T. H. Lin, *et al.*, "Loihi: A neuromorphic manycore processor with on-chip learning," IEEE Micro **38**, 82–99 (2018).
11. J. Pei, L. Deng, S. Song, *et al.*, "Towards artificial general intelligence with hybrid Tianjic chip architecture," Nature **572**, 106–111 (2019).
12. G. Wetzstein, A. Ozcan, S. Gigan, S. Fan, D. Englund, M. Soljačić, C. Denz, D. A. B. Miller, and D. Psaltis, "Inference in artificial intelligence with deep optics and photonics," Nature **588**, 39–47 (2020).
13. B. J. Shastri, A. N. Tait, T. Ferreira de Lima, W. H. Pernice, H. Bhaskaran, C. D. Wright, and P. R. Prucnal, "Photonics for artificial intelligence and neuromorphic computing," Nat. Photonics **15**, 102–114 (2021).
14. S. Xiang, Y. Han, Z. Song, X. Guo, Y. Zhang, Z. Ren, S. Wang, Y. Ma, W. Zou, and B. Ma, "A review: Photonics devices, architectures, and algorithms for optical neural computing," J. Semicond. **42**, 023105 (2021).
15. H. Zhou, J. Dong, J. Cheng, W. Dong, C. Huang, Y. Shen, Q. Zhang, M. Gu, C. Qian, H. Chen, Z. Ruan, and X. Zhang, "Photonic matrix multiplication lights up photonic accelerator and beyond," Light Sci. Appl. **11**, 30 (2022).
16. C. Huang, V. J. Sorger, M. Miscuglio, M. Al-Qadasi, A. Mukherjee, L. Lampe, M. Nichols, A. N. Tait, T. Ferreira de Lima, B. A. Marquez, J. Wang, L. Chrostowski, M. P. Fok, D. Brunner, S. Fan, S. Shekhar, P. R. Prucnal, and B. J. Shastri, "Prospects and applications of photonic neural networks," Adv. Phys. X **7**, 1981155 (2022).
17. P. R. Prucnal, B. J. Shastri, T. F. de Lima, M. A. Nahmias, and A. N. Tait, "Recent progress in semiconductor excitable lasers for photonic spike processing," Adv. Opt. Photon. **8**, 228–299 (2016).
18. X. Guo, J. Xiang, Y. Zhang, and Y. Su, "Integrated neuromorphic photonics: synapses, neurons, and neural networks," Adv. Photon. Res. **2**, 2000212 (2021).
19. X. Lin, Y. Rivenson, N. T. Yardimci, M. Veli, Y. Luo, M. Jarrahi, and A. Ozcan, "All-optical machine learning using diffractive deep neural networks," Science **361**, 1004–1008 (2018).
20. T. K. Zhou, X. Lin, J. Wu, Y. Chen, H. Xie, Y. Li, J. Fan, H. Wu, L. Fang, and Q. Dai, "Large-scale neuromorphic optoelectronic computing with a reconfigurable diffractive processing unit," Nat. Photonics **15**, 367–373 (2021).
21. Y. Shen, N. C. Harris, S. Skirlo, M. Prabhu, T. Baehr-Jones, M. Hochberg, X. Sun, S. Zhao, H. Larochelle, D. Englund, and M. Soljačić, "Deep learning with coherent nanophotonic circuits," Nat. Photonics **11**, 441–446 (2017).
22. A. N. Tait, T. Ferreira de Lima, E. Zhou, A. X. Wu, M. A. Nahmias, B. J. Shastri, and P. R. Prucnal, "Neuromorphic photonic networks using silicon photonic weight banks," Sci. Rep. **7**, 7430 (2017).
23. J. Feldmann, N. Youngblood, C. D. Wright, H. Bhaskaran, and W. H. Pernice, "All-optical spiking neurosynaptic networks with self-learning capabilities," Nature **569**, 208–214 (2019).
24. J. Feldmann, N. Youngblood, M. Karpov, H. Gehring, X. Li, M. Stappers, M. Le Gallo, X. Fu, A. Lukashchuk, A. S. Raja, J. Liu, C. D. Wright, A. Sebastian, T. J. Kippenberg, W. H. P. Pernice, and H. Bhaskaran, "Parallel convolutional processing using an integrated photonic tensor core," Nature **589**, 52–58 (2021).
25. S. Xiang, Y. Zhang, J. Gong, X. Guo, L. Lin, and Y. Hao, "STDP-based unsupervised spike pattern learning in a photonic spiking neural network with VCSELs and VCSOAs," IEEE J. Sel. Top. Quantum Electron. **25**, 1700109 (2019).
26. S. Xiang, Z. Ren, Z. Song, Y. Zhang, X. Guo, G. Han, and Y. Hao, "Computing primitive of fully VCSEL-based all-optical spiking neural network for supervised learning and pattern classification," IEEE Trans. Neural Netw. Learn. Syst. **32**, 2494–2505 (2021).
27. B. Shi, N. Calabretta, and R. Stabile, "Deep neural network through an InP SOA-based photonic integrated cross-connect," IEEE J. Sel. Top Quant. Electron. **26**, 7701111 (2020).
28. X. Xu, M. Tan, B. Corcoran, J. Wu, A. Boes, T. G. Nguyen, S. T. Chu, B. E. Little, D. G. Hicks, R. Morandotti, A. Mitchell, and D. J. Moss, "11 TOPS photonic convolutional accelerator for optical neural networks," Nature **589**, 44–51 (2021).
29. S. Xu, J. Wang, H. Shu, Z. Zhang, S. Yi, B. Bai, X. Wang, J. Liu, and W. Zou, "Optical coherent dot-product chip for sophisticated deep learning regression," Light Sci. Appl. **10**, 1–12 (2021).
30. H. Zhang, M. Gu, X. D. Jiang, J. Thompson, H. Cai, S. Paesani, R. Santagati, A. Laing, Y. Zhang, M. H. Yung, Y. Z. Shi, F. K. Muhammad, G. Q. Lo, X. S. Luo, B. Dong, D. L. Kwong, L. C. Kwek, and A. Q. Liu, "An optical neural chip for implementing complex-valued neural network," Nat. Commun. **12**, 1–11 (2021).
31. Y. Tian, Y. Zhao, S. Liu, Q. Li, W. Wang, J. Feng, and J. Guo, "Scalable and compact photonic neural chip with low learning-capability-loss," Nanophotonics **11**, 329–344 (2022).
32. Z. Song, S. Xiang, Z. Ren, S. Wang, A. Wen, and Y. Hao, "Photonic spiking neural network based on excitable VCSELs-SA for sound azimuth detection," Opt. Express **28**, 1561–1573 (2020).
33. Y.-J. Lee, M. Berkay On, X. Xiao, R. Proietti, and S. J. Ben Yoo, "Photonic spiking neural networks with event-driven femtojoule optoelectronic neurons based on Izhikevich-inspired model," Opt. Express **30**, 19360–19389 (2022).
34. Z. Song, S. Y. Xiang, S. Zhao, Y. Zhang, X. Guo, Y. Tian, Y. Shi, and Y. Hao, "A hybrid-integrated photonic spiking neural network framework based on an MZI Array and VCSELs-SA," IEEE J. Sel. Top. Quantum Electron. **29**, 8300211 (2023).
35. W. Coomans, L. Gelens, S. Beri, J. Danckaert, and G. Van der Sande, "Solitary and coupled semiconductor ring lasers as optical spiking neurons," Phys. Rev. E **84**, 036209 (2011).
36. A. Hurtado, K. Schires, I. D. Henning, and M. J. Adams, "Investigation of vertical cavity surface emitting laser dynamics for neuromorphic photonic systems," Appl. Phys. Lett. **100**, 103703 (2012).
37. J. Robertson, E. Wade, Y. Kopp, Y. Bueno, and A. Hurtado, "Toward neuromorphic photonic networks of ultrafast spiking laser neurons," IEEE J. Sel. Top. Quantum Electron. **26**, 7700715 (2020).

38. T. Deng, J. Robertson, and A. Hurtado, "Controlled propagation of spiking dynamics in vertical-cavity surface-emitting lasers: towards neuromorphic photonic networks," IEEE J. Sel. Top. Quantum Electron. **23**, 1800408 (2017).
39. B. J. Shastri, M. A. Nahmias, A. N. Tait, A. W. Rodriguez, B. Wu, and P. R. Prucnal, "Spiking processing with a graphene excitable laser," Sci. Rep. **6**, 19126 (2016).
40. M. A. Nahmias, B. J. Shastri, A. N. Tait, and P. R. Prucnal, "A leaky integrate-and-fire laser neuron for ultrafast cognitive computing," IEEE J. Sel. Top. Quantum Electron. **19**, 1800212 (2013).
41. A. Jha, C. Huang, H.-T. Peng, B. Shastri, and P. R. Prucnal, "Photonic spiking neural networks and graphene-on-silicon spiking neurons," J. Lightwave Technol. **40**, 2901–2914 (2022).
42. I. Chakraborty, G. Saha, G. Sengupta, and K. Roy, "Toward fast neural computing using all-photonic phase change spiking neurons," Sci. Rep. **8**, 12980 (2018).
43. F. Selmi, R. Braive, G. Beaudoin, I. Sagnes, R. Kuszelewicz, and S. Barbay, "Relative refractory period in an excitable semiconductor laser," Phys. Rev. Lett. **112**, 183902 (2014).
44. V. A. Pammi, K. Alfaro-Bittner, M. G. Clerc, and S. Barbay, "Photonic computing with single and coupled spiking micropillar lasers," IEEE J. Sel. Top. Quantum Electron. **26**, 1500307 (2020).
45. H. T. Peng, G. Angelatos, T. F. de Lima, M. A. Nahmias, A. N. Tait, S. Abbaslou, B. J. Shastri, and P. R. Prucnal, "Temporal information processing with an integrated laser neuron," IEEE J. Sel. Top. Quantum Electron. **26**, 5100209 (2020).
46. J. Xiang, Y. Zhang, Y. Zhao, X. Guo, and Y. Su, "All-optical silicon micro-ring spiking neuron," Photon. Res. **10**, 939–946 (2022).
47. L. Hou, M. Haji, J. Akbar, B. Qiu, and A. C. Bryce, "Low divergence angle and low jitter 40 GHz AlGaInAs/InP 1.55 μm mode-locked lasers," Opt. Lett. **36**, 966–968 (2011).
48. R. Gütig and H. Sompolinsky, "The tempotron: a neuron that learns spike timing–based decisions," Nat. Neurosci. **9**, 420–428 (2006).
49. F. Ponulak and A. Kasiński, "Supervised learning in spiking neural networks with ReSuMe: sequence learning, classification, and spike shifting," Neural Comput. **22**, 467–510 (2010).
50. J. L. Dubbeldam and B. Krauskopf, "Self-pulsations of lasers with saturable absorber: dynamics and bifurcations," Opt. Commun. **159**, 325–338 (1999).
51. D. J. Jones, L. M. Zhang, J. E. Carroll, and D. D. Marcenac, "Dynamics of monolithic passively mode-locked semiconductor lasers," IEEE J. Quantum Electron. **31**, 1051–1058 (1995).
52. S. Wieczorek, B. Krauskopf, T. B. Simpson, and D. Lenstra, "The dynamical complexity of optically injected semiconductor lasers," Phys. Rep. **416**, 1–128 (2005).
53. N. Lindenmann, G. Balthasar, D. Hillerkuss, R. Schmogrow, M. Jordan, J. Leuthold, W. Freude, and C. Koos, "Photonic wire bonding: a novel concept for chip-scale interconnects," Opt. Express **20**, 17667–17677 (2012).
54. Y. Shi, S. Li, X. Chen, L. Li, J. Li, T. Zhang, J. Zheng, Y. Zhang, S. Tang, L. Hou, J. H. Marsh, and B. Qiu, "High channel count and high precision channel spacing multi-wavelength laser array for future PICs," Sci. Rep. **4**, 7377 (2014).